

Applications of the Boundary Element Method in Electrochemistry: Scanning Electrochemical Microscopy, Part 2

Q. Fulian and A. C. Fisher*

Department of Chemistry, University of Bath, Claverton Down, Bath BA2 7AY, U.K.

G. Denuault

Department of Chemistry, University of Southampton, Highfield, Southampton, SO17 1BJ, U.K.

Received: October 7, 1998

Boundary element method (BEM) simulations are presented for a range of scanning electrochemical microscopy applications. Calculations are performed to quantify the effects of the surrounding shield for a range of tip geometries and produce three-dimensional images of electrodes embedded in substrate surfaces. Approach curves are presented for a range of experimentally exploited probes, including the sphere–cap electrode. In addition, the BEM is used to generate a line scan across the interface between a conducting and nonconducting substrate for different tip geometries. The comparative resolution at a fixed tip–substrate separation for a microdisk and microhemisphere probe is noted. Finally, three-dimensional images of raised and recessed hemispherical electrodes embedded in nonconducting flat substrates are generated and the results compared to the image of a microdisk electrode.

Introduction

The development of scanning electrochemical microscopy (SECM) in the late 1980s^{1–12} has led to a significant leap in the understanding of chemical reactivity occurring at the solid–liquid interface. Analytical and numerical methods have been applied to quantify the data produced to ascertain quantitative mechanistic and kinetic parameters. However, most of the approaches applied up to recent times have assumed an axisymmetric (two-dimensional) model, owing to the complexity of the problems addressed. Numerical techniques such as the finite difference method (FDM) have been used to quantify approach curves under idealized working conditions (e.g., perfectly flat substrates, etc.), but owing to the point approximation employed and the necessity to employ iterative methods, the scope for expansion of these techniques to complex geometries in two and three dimensions is significantly limited by simulation time and memory requirements. More recently, we have demonstrated^{13–15} that the boundary element method (BEM) and finite element method (FEM)^{16–20} can be employed to overcome many of the limitations of the analytical and FDM models. In the case of the BEM this only requires the boundary of the domain to be modeled. Thus, a two-dimensional problem is rendered effectively one-dimensional for numerical solution. In addition, the approach allows the steady-state solution to be obtained in a single step rather than the need for time-consuming and unnecessary iteration often required by the FDM.

In this paper we continue the development of the BEM for SECM applications. Specifically, we explore the effect of the shield size around a variety of probe electrode shapes. This problem has received limited attention up to now in the literature yet is simply tackled using the BEM. In addition, we present approach curves for the sphere–cap probe geometry, which has previously only been approximated using analytical theory.²² Again, the influence of shield geometry is addressed for this probe. In addition, we explore the resolution of different SECM

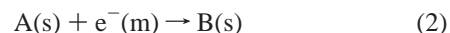
probes by modeling a single line scan across the boundary between a large conducting and large nonconducting interface. The line scan is presented for a disk and hemisphere tip electrode geometry using a fixed tip–substrate separation. Finally, we use three-dimensional simulations to produce images of microelectrodes embedded in large insulating substrates. Specifically, we examine the effect of distorting a microdisk electrode to a raised and recessed hemispherical object and examine the overlap of the diffusion fields around two microelectrodes operating in positive feedback mode.

Theory

We have previously presented¹³ the background theory for the formulation of steady-state one-, two-, and three-dimensional solutions of the diffusion eq 1 pertinent to electrolysis under conditions of high supporting electrolyte.

$$D\left(\frac{\partial^2 c}{\partial x^2}\right) + D\left(\frac{\partial^2 c}{\partial y^2}\right) + D\left(\frac{\partial^2 c}{\partial z^2}\right) = 0 \quad (1)$$

We therefore restrict our discussion here to a brief outline of our general approach. In this paper we shall consider the current response for the reversible one-electron-transfer reaction



For the purposes of SECM calculations we adopt an identical strategy to that presented previously.¹⁵ The SECM tip electrode induces the transport-limited reduction of A at the electrode surface. For substrates operating in positive feedback mode¹ the reverse of the SECM tip reaction is induced at the substrate surface. In all cases presented the normalization procedures adopted are identical to those employed by Kwak and Bard.¹

The BEM allows expressions such as eq 1 to be reduced to a boundary-only problem by selection and integration of

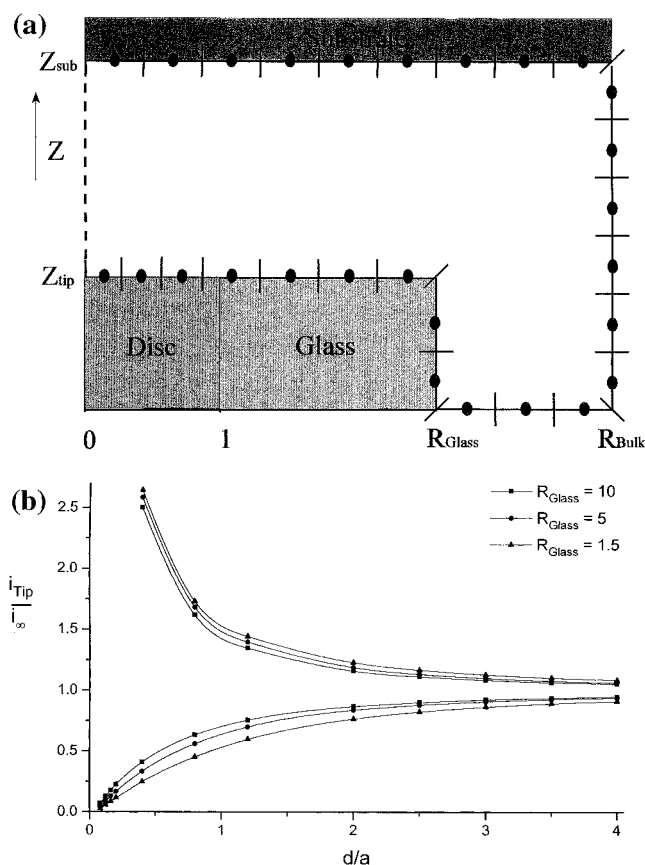


Figure 1. (a) Schematic of the BEM grid and geometry employed for microdisk approach curve simulations using variable sheath sizes. (b) Dimensionless approach curves for hindered and positive feedback modes for a microdisk electrode approaching a flat substrate, for different sheath radii (R_{glass}). Also shown in the plot are the values (●, ▲, and □) presented previously in ref 21.

appropriate weighting functions G . For the three-dimensional form of eq 1 the integration procedure is performed over x , y , and z coordinates and the fundamental solution satisfies

$$\frac{\partial^2 G}{\partial x^2} + \frac{\partial^2 G}{\partial y^2} + \frac{\partial^2 G}{\partial z^2} = -\delta(x - \xi_1)(y - \xi_2)(z - \xi_3) \quad (3)$$

where ξ_1 , ξ_2 , and ξ_3 represent the coordinates of a concentration source. The weighting function is selected as

$$G(x, y, z, \xi_1, \xi_2, \xi_3) = \frac{1}{4\pi r} \quad (4)$$

where r is the distance between the integration point and the source point,

$$r = ((x - \xi_1)^2 + (y - \xi_2)^2 + (z - \xi_3)^2)^{1/2} \quad (5)$$

Numerical solution proceeds by mapping the boundary of the domain into a series of (boundary) elements. As previously, we have employed triangular elements¹³ for these simulations, which take a single fixed flux or concentration over each individual element. The size of the surrounding sheath on the tip is designated G_{glass} , which is consistent with previous publications.²¹ The variable d/a is employed to represent the normalized tip-substrate ($Z_{\text{tip}} - Z_{\text{sub}}$) separation as depicted in Figure 1a. All routines were written in Fortran 77 or 90 and run on a Pentium 166 PC, with 48 MB Ram. Run times varied

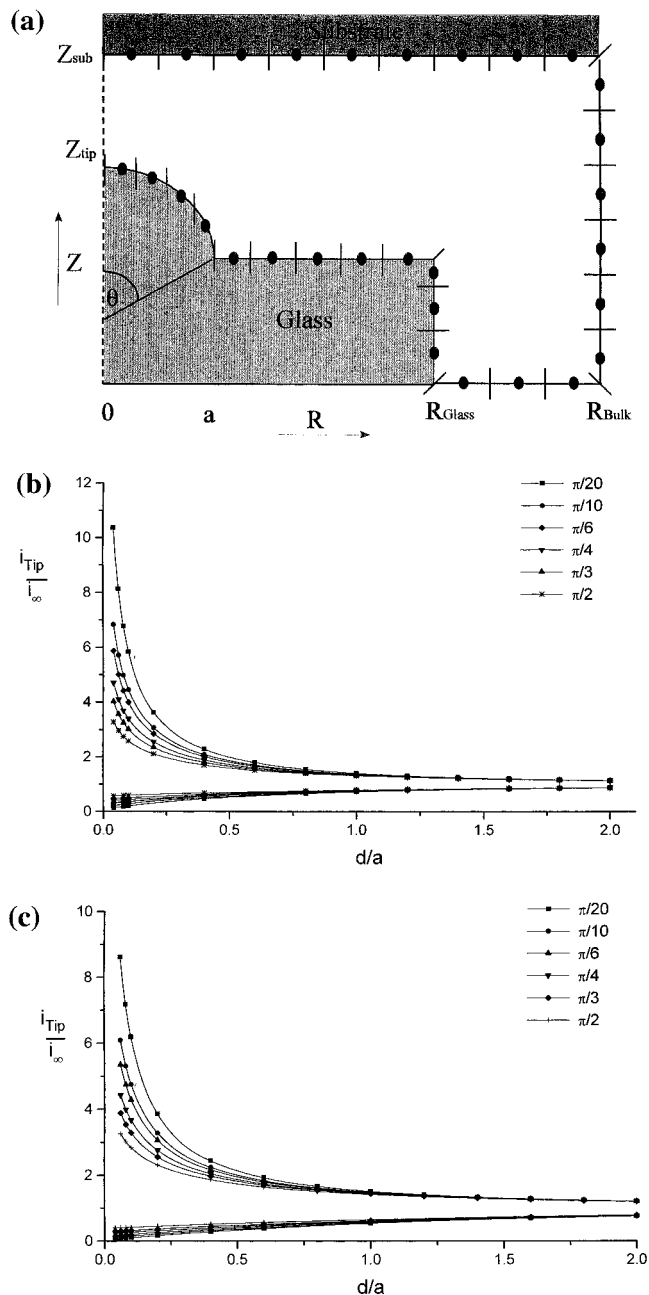


Figure 2. (a) Schematic of the BEM grid and geometry employed for microhemispherical approach curve simulations. (b) Dimensionless approach curves for hindered and positive feedback modes using microhemispherical electrode geometries generated for different values of θ and $R_{\text{glass}} = 2$. (c) Dimensionless approach curves for hindered and positive feedback modes using microhemispherical electrode geometries generated for different values of θ and $R_{\text{glass}} = 7$.

between 1 and 20 min for a single steady-state current measurement, depending upon the problem of interest.

Results and Discussion

Two-Dimensional Simulations. Initial simulations focused on the application of the two-dimensional (axisymmetric) codes to examine the current response of a microdisk of normalized radius 1 embedded within a flat insulating sheath of varying normalized radius (R_{glass}) as it was stepped toward a flat conducting or nonconducting substrate. The domain of interest was divided into 50 boundary elements (Figure 1a), and the following boundary conditions were applied. Figure 1b shows

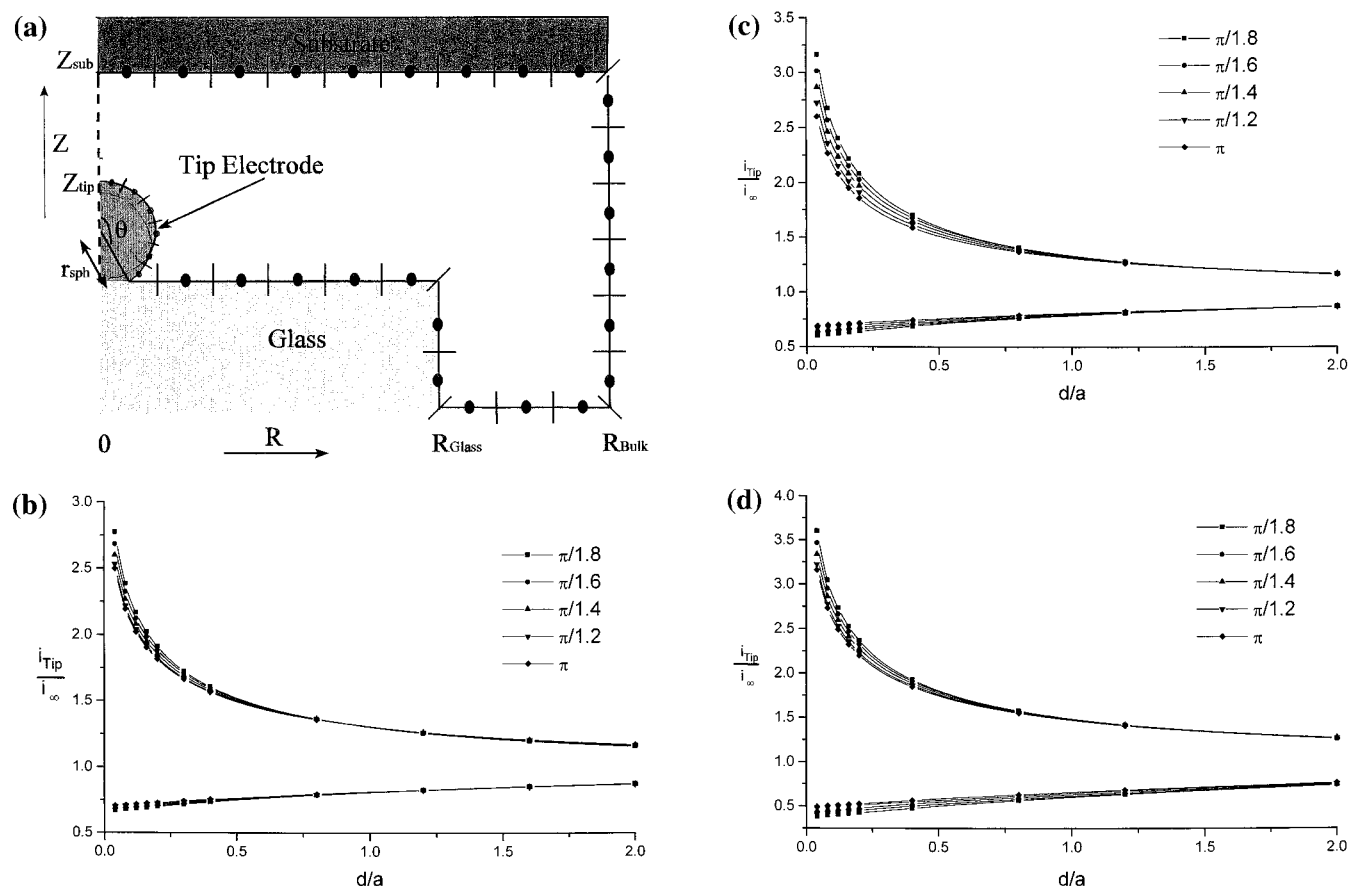


Figure 3. (a) Schematic of the BEM grid and geometry employed for microsphere–cap approach curve simulations. (b) Dimensionless approach curves for hindered and positive feedback modes for microsphere–cap electrodes generated for different values of θ , using $R_{glass} = 1$. (c) Dimensionless approach curves for hindered and positive feedback modes for microsphere–cap electrodes generated for different values of θ , using $R_{glass} = 2$. (d) Dimensionless approach curves for hindered and positive feedback modes for microsphere–cap electrodes generated for different values of θ , using $R_{glass} = 11$.

region		insulating substrate	conducting substrate
$1 > r > 0$	$Z = Z_{tip}$	$[A] = 0$	$[A] = 0$
$r = R_{bulk}$	$Z_{sub} > z > Z_{tip}$	$[A] = 1$	$[A] = 1$
$R_{bulk} > r > 0$	$Z = Z_{sub}$	$\partial[A]/\partial Z = 0$	$[A] = 1$
$R_{bulk} > r > 1$	$Z = Z_{tip}$	$\partial[A]/\partial Z = 0$	$\partial[A]/\partial Z = 0$
$r = 0$	$Z_{sub} > z > Z_{tip}$	$\partial[A]/\partial R = 0$	$\partial[A]/\partial R = 0$

the normalized current response as a function of R_{glass} . Also shown in the figure are the results predicted using a finite difference model,²¹ recently reported by the Southampton group. It is apparent that excellent agreement is noted between the two approaches for each sheath size examined. The origin of the variation of normalized current arises from the enhanced transport to the tip electrode as the sheath is progressively decreased in size.

We repeated the above procedures for the case of a range of microhemispherical geometries (Figure 2a) generated using an approach identical to that reported previously for the case of an infinite sheath radius.¹⁵ Parts b and c of Figure 2 show the corresponding results for hindered and positive feedback modes using sheath sizes of $R_{glass} = 2$ and $R_{glass} = 7$. In this case the influence of sheath size is found to be most significant for geometries that are close in form to the disk ($\theta = \pi/2$) and becomes increasingly less important as the geometry approaches the case of a true hemisphere ($\theta = 0$). This may be rationalized owing to the shape of the diffusion layer created around the tip region. In the case of the hemisphere the contours of concentration follow the electrode surface, and so there is not the enhanced current density observed at a microdisk electrode edge.

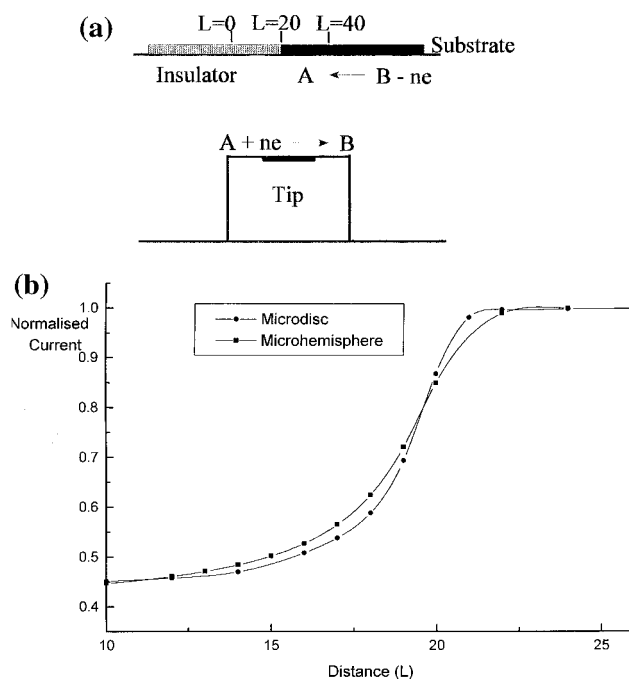


Figure 4. (a) Schematic of the geometry employed for a line scan simulation using a microdisk or microhemisphere electrode. (b) Line scan recorded for a microdisk and microhemisphere tip electrode for the geometry depicted in part a.

This in turn leads to the hemispherical geometry being less perturbed by the influence of the sheath radius.

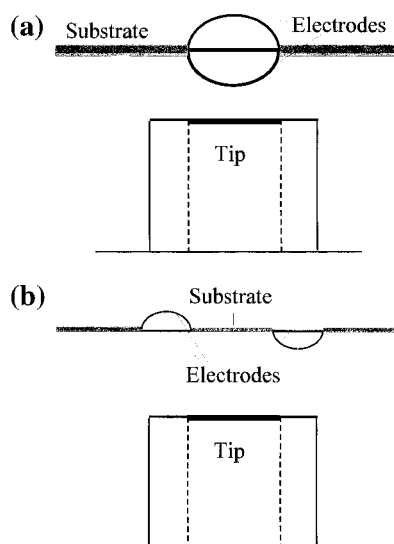


Figure 5. Schematics of the geometries employed for image simulations (a) of single microelectrodes and (b) double microelectrodes, operating in positive feedback mode.

Next we examined the approach curve response for a sphere-cap tip electrode of varying geometry (Figure 3a). The different

spherical electrodes were generated using various values of θ and r_{sph} . Three different normalized sheath radii were employed ($R_{\text{glass}} = 1$, $R_{\text{glass}} = 2$, and $R_{\text{glass}} = 11$) using $r_{\text{sph}} = 1$, and the results are presented in parts b–d of Figure 3. It is apparent that the sheath size significantly alters the response of the approach curves in both hindered and positive feedback modes. Again, the effects arise from the enhancement in transport to the tip electrode as the sheath size is decreased.

Three-Dimensional Simulations. Having established the influence of sheath size on a range of electrode tip geometries, the next simulations were performed to examine the relative resolution of a microhemisphere and microdisk electrode (both of normalized radius 1) tip electrodes. The case examined is depicted in Figure 4a; the tip electrode is positioned at various points across the boundary between a flat macroelectrode (operating in positive feedback mode) and a flat insulator. The line scan was recorded using a fixed substrate–tip separation (d/a) of normalized distance 1, and Figure 4b shows the result of the simulation where each of the normalized currents ($i_{\text{tip}}/i_{\infty}$) for the microdisk and microhemisphere electrodes have been divided by their values at the position $L = 25$. It is apparent that the two tip shapes show very similar behavior. However, there is a slight broadening of the response for the microhemi-

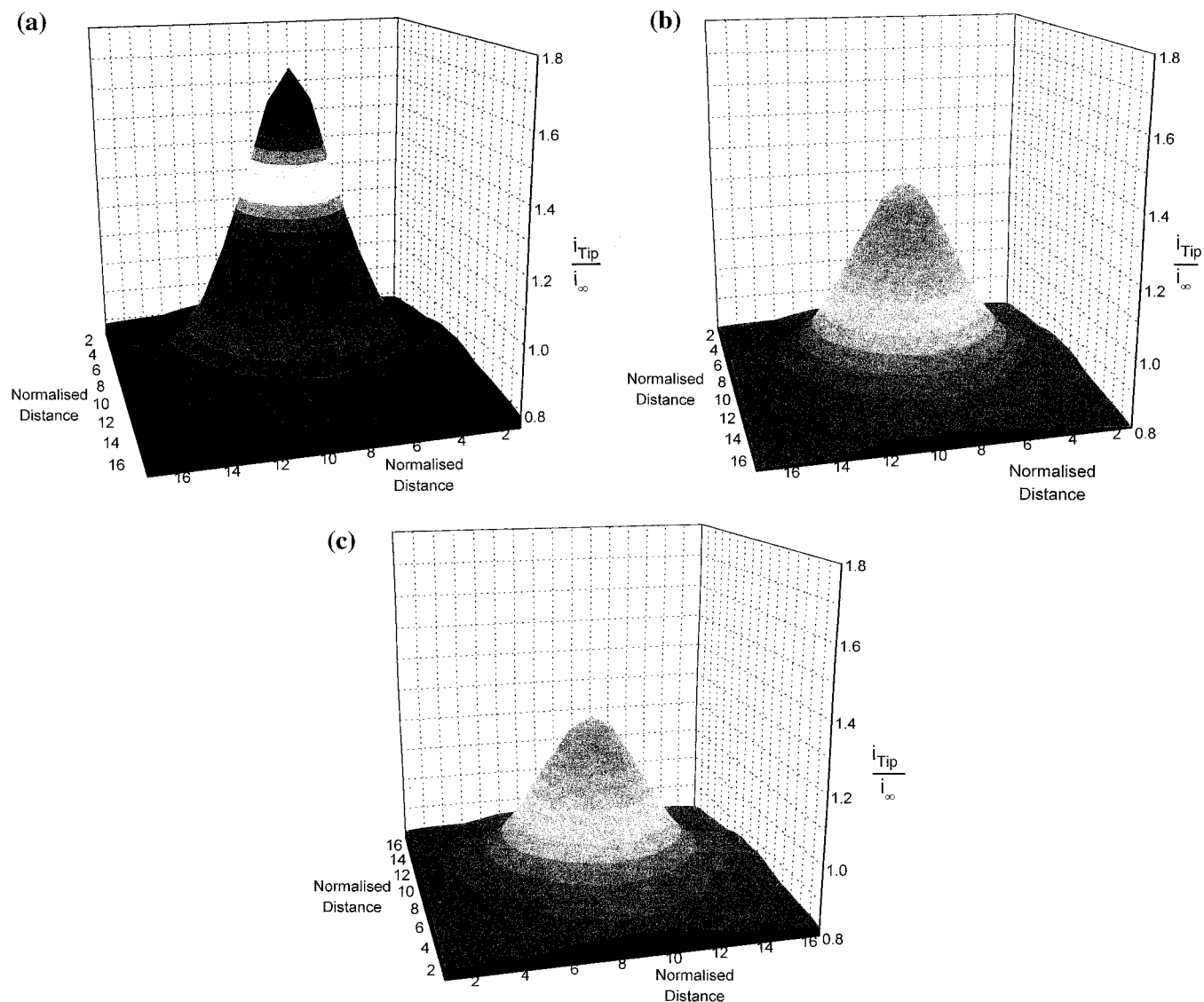


Figure 6. SECM images recorded using single electrodes embedded in a flat substrate, using (a) a raised hemispherical type electrode, (b) a flat microdisk electrode, and (c) a recessed hemispherical type electrode.

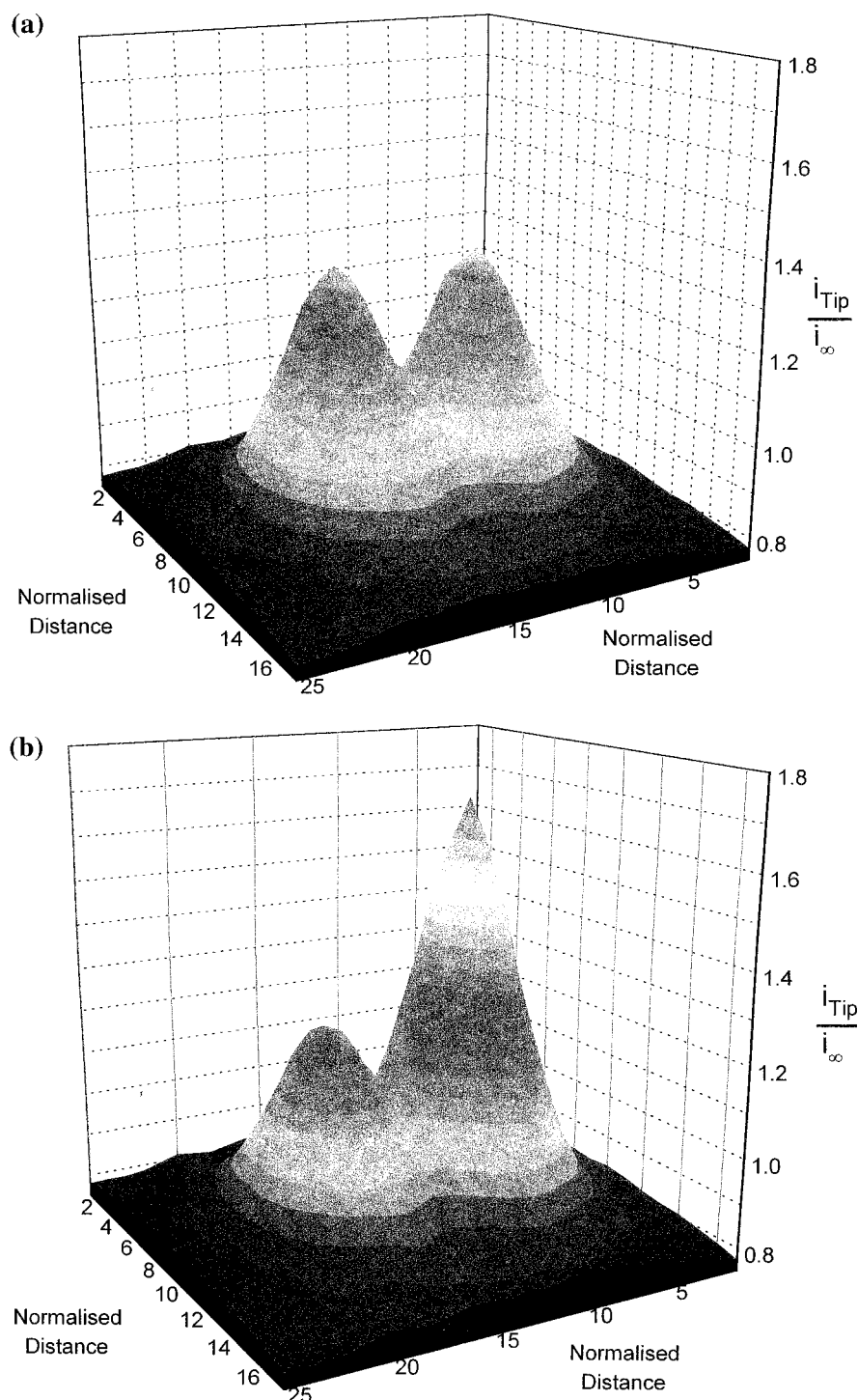


Figure 7. SECM images recorded using double electrodes embedded in a flat substrate, using (a) both electrodes as microdisks and (b) one microhemispherical electrode raised and one recessed.

spherical electrode. Thus, under the conditions considered, the disk has a slightly higher resolving power than the hemisphere.

Finally, three-dimensional BEM simulations were performed to obtain images of microelectrodes operating in positive feedback mode embedded in flat nonconducting substrates. A schematic of the problems addressed are shown in Figure 5. First, single-substrate electrodes were examined (Figure 5a) with the normalized substrate–tip separation (d/a) set at 1. Figure 6 shows the resulting images obtained using a microdisk tip electrode as the probe in a flat nonconducting sheath of normalized radius 10. The three images presented correspond to a raised hemispherical object ($h = 0.5$, $r_{\text{hem}} = 1$), a flat disk

(radius = 1), and a recessed hemispherical object ($h = 0.5$, $r_{\text{hem}} = 1$) where the parameters h and r_{hem} have been defined previously.¹⁵ The images were constructed as noted previously using 100 separate steady-state measurements across the substrate surface. On each image the center of the substrate electrode is positioned at the normalized coordinates $x = 8$, $y = 8$. For clarity the z scale has been set identically for each plot. Each image shows a symmetrical hemispherical field resulting from the feedback diffusion at each of the substrate electrodes. The magnitude of the signal, however, varies considerably between the three cases. Although the hemispherical objects have only been raised (or recessed) by half of the

tip radius, it is apparent that the SECM images show substantial variation. This highlights the topographical sensitivity of the technique when positive feedback mode is employed.

The final images recorded were for multiple electrode arrangements (Figure 5b); in this case two microelectrodes were embedded in the substrate. The same procedures and conditions were employed as above with both electrodes operating in positive feedback mode. Figure 7a shows the results for two flat disk electrodes separated by a normalized distance of 2. The overlap of the diffusional fields around each electrode is apparent from the images, and the maximum current at each is consequently less than that noted for the single disk electrode image (Figure 6b).

Next the procedure was repeated for a raised and recessed microhemispherical electrode separated by the same distance as above and using parameters for the hemispherical distortion identical to those used to generate parts a and c of Figure 6. Again, the same z scale as Figure 7a was used to highlight the relative magnitudes of the signals obtained from the two geometries. As was noted in Figure 7a, the diffusional fields from the two electrodes can be seen to overlap, but the maxima are considerably different from the single-electrode cases. Also, the image reveals the sensitivity of the SECM to resolve objects situated close to one another operating in positive feedback mode.

Conclusion

The BEM has been employed to characterize the current density of a number of experimentally interesting electrode geometries under diffusional mass transport control. The approach has been demonstrated as a flexible and efficient tool for the examination of the current flow as a function of the geometrical influence of electrodes and surrounding insulating regions. The ease of application to electrodes of arbitrary geometry offers the possibility of mapping true experimental

electrode shapes via scanning probe techniques and simulating the expected response rather than assuming the systems to be idealized shapes contained within a flat surrounding insulator.

Acknowledgment. We thank the University of Bath for a University Studentship for support of Q.F.

References and Notes

- (1) Bard, A. J.; Fan, F. R. F.; Kwak, J.; Lev, O. *Anal. Chem.* **1989**, *61*, 132.
- (2) Bard, A. J.; Denuault, G.; Lee, C.; Mandler, D.; Wipf, D. O. *Acc. Chem. Res.* **1990**, *23*, 357.
- (3) Denuault, G.; Mirkin, M. V.; Bard, A. J. *J. Electroanal. Chem.* **1991**, *86*, 27.
- (4) Mirkin, M. V.; Fan, F. R. F.; Bard, A. J. *J. Electroanal. Chem.* **1992**, *328*, 47.
- (5) Bard, A. J.; Mirkin, M. V.; Unwin, P. R.; Wipf, D. O. *J. Phys. Chem.* **1992**, *96*, 1861.
- (6) Bard, A. J.; Fan, F. R. F.; Mirkin, M. V. *Electroanal. Chem.* **1994**, *18*, 243.
- (7) Arca, M.; Bard, A. J.; Horrocks, B. R.; Richards, T. C.; Treichel, D. A. *Analyst* **1994**, *119*, 719.
- (8) Fan, F. R. F.; Bard, A. J. *Science* **1995**, *267*, 871.
- (9) Wei, C.; Bard, A. J.; Mirkin, M. V. *J. Phys. Chem.* **1995**, *99*, 16033.
- (10) Tsionsky, M.; Bard, A. J.; Mirkin, M. V. *J. Phys. Chem.* **1996**, *100*, 17881.
- (11) Mirkin, M. V. *Anal. Chem.* **1996**, *68*, 177A.
- (12) Shao, Y.; Mirkin, M. V.; Rusling, J. F. *J. Phys. Chem. B* **1997**, *101*, 3202.
- (13) Fulian, Q.; Fisher, A. C. *J. Phys. Chem. B*, in press.
- (14) Fulian, Q.; Fisher, A. C. *J. Phys. Chem. B*, manuscript submitted.
- (15) Fulian, Q.; Fisher, A. C.; Denuault, G. *J. Phys. Chem. B* **1999**, *103*, 4387.
- (16) Stevens, N. P. C.; Fisher, A. C. *J. Phys. Chem.* **1997**, *101*, 8259.
- (17) Stevens, N. P. C.; Fisher, A. C. *Electroanalysis* **1997**, *10*, 16.
- (18) Stevens, N. P. C.; Fisher, A. C. *J. Ann. Chim.* **1997**, *93*, 225.
- (19) Fulian, Q.; Stevens, N. P. C.; Fisher, A. C. *J. Phys. Chem. B* **1998**, *102*, 3779.
- (20) Stevens, N. P. C.; Gooch, K. A.; Fulian, Q.; Fisher, A. C.; Compton, R. G. *Anal. Chem.*, manuscript submitted.
- (21) Amphlett, J. L.; Denuault, G. *J. Phys. Chem.* **1998**, *102*, 9946.
- (22) Demaille, C.; Brust, M.; Tsionsky, M.; Bard, A. J. *Anal. Chem.* **1997**, *69*, 2323.